Preliminary CFD Validation of Unsteady Onflow Effects on Model Train Drag

Keith A. Weinman(✉) and Klaus Ehrenfried

DLR Göttingen, Institute of Aerodynamics and Flow Technology,
Bunsenstr. 10, 37073 Göttingen, Germany
keith.weinman@dlr.de

Abstract. The DLR New Generation Train Cargo concept (NGT-Cargo) aims to increase the rail share of the European freight traffic market. Computational Fluid Dynamics (CFD) is a useful tool in analyzing high-speed operations which are an important part of this concept. The development of aerodynamic forces under unsteady on-flows should be analyzed within the context of industrial standards, for example guidelines are provided for CFD assessments at cross-wind conditions using the RANS (Reynolds-averaged Navier-Stokes) equations. A major challenge arises because the multi-scale nature of these flows are characterized by a large range of energetically significant flow scales. Wind-tunnel measurements, focused on the development of the aerodynamic forces acting on a train, are being currently performed on a 1:25 scaled NGT model in the cross-wind facility *Seitenwindversuchsanlage* Göttingen (SWG) located at the DLR Göttingen. This paper presents preliminary work assessing the ability of CFD to reproduce both the observed on-flow conditions as well as the aerodynamic drag of the vehicle.

1 Introduction

Stringent safety requirements over a wide range of operational conditions are applied to modern high-speed trains. Achieving this requires an understanding of the aerodynamic forces under cross-wind conditions. Measurement of force coefficients for full-scale vehicles is optimal but it is expensive. Normal practice is geared towards the use of small-scale models that can be tested inexpensively in wind-tunnel experiments or by using full-scale in-service vehicles [1]. Vehicle stability is of paramount importance, but accurate assessments of vehicle aerodynamic forces under realistic atmospheric conditions are now becoming relevant. The use of computational methods to assess the aerodynamic loading on trains has been recognized by the transport industry. The German standard EN 14067-6 [3] permits evaluation of aerodynamic forces for cross-wind conditions using CFD simulations for full-scale or reduced model geometries. Guidelines in EN 14067-6 for Reynolds Averaged Navier-Stokes (RANS) methods are stringent: computed integral forces cannot be accepted for certification work if variations against an accepted reference value differs by more than three percent. Computational assessments of the flow about a train, traditionally undertaken on the

A. Dillmann et al. (Eds.): STAB/DGLR Symposium 2022, NNFM 154, pp. 294–304, 2024.
https://doi.org/10.1007/978-3-031-40482-5_28

basis of RANS methods, have not been satisfactory. For example [10] and [11] compared computational estimates of integral forces and moments using well-resolved meshes against the NGT2 experiment of [12]. Computations were performed for Reynolds numbers in the range $R \in [250000, 750000]$ with cross-wind conditions of up to 30°. Computed aerodynamic force and moment coefficients, particularly drag, demonstrated differences against experimental measurements of up to 15%. Improvements in vehicle force moment estimations have been demonstrated with improvements in physical modeling [8,11,13], however drag estimates remain unsatisfactory. A significant challenge is provided by the multi-scale nature of flows characterized by a large range of energetically significant length scales. Geometrical features of a train, such as the underflow region, the train base [4,5], the inter-car gaps (ICG's) and bogie cavities, generate small-scale unsteady flow structures which interact with larger flow scales and can thereby influence the development of the aerodynamic forces. [4] observed that traditional RANS methods will retain their importance for the foreseeable future. This observation provided the motivation for a study on meshing requirements for RANS methods [9]. This study identifies the front nose of the vehicle as a critical refinement area with other regions being of secondary importance. Minor modifications of these recommendations, with the aim of extending them to unsteady flows, are made in the present paper.

Vehicle aerodynamic loading under unsteady conditions were studied experimentally in [14] and [15]. Measurements were collected in-field under real conditions. Wind-tunnel experiments using a flapped system to control model on-flow length and time scales were also undertaken. Two CFD methods were developed and validated against both of these experimental approaches [16]. The first method uses mesh free reconstruction methods to construct on-flow boundary conditions that are representative of measured flow length and time scales. A second method, upon which the work in this paper is based, used sliding mesh techniques to model a set of oscillating flaps. The paper is organized as follows: A brief overview of the train model is presented in Sect. 2. The numerical method is discussed in Sect. 3. A short overview of the mesh is then introduced in Sect. 4. This is following by a discussion on the comparison of the computational and experimental results. Conclusions are presented in Sect. 6 respectively.

2 Details on the Train Model and Experiment

For this paper a model consisting only of the main train aerodynamic surfaces and the wind tunnel is considered. Features, such as the inter-car gaps and bogey cavities, are also included. Figure 1(a) illustrates the computational model. The main components include the model, the wind tunnel (with nozzle, test section, and diffuser), as well as the room within which the wind tunnel is located. The origin of the coordinate system used both for the experiment and the CFD is illustrated at the start of the test section at $\mathbf{x} = (\mathbf{0}, \mathbf{0}, \mathbf{0})$). Figure 1(b) illustrates the flapped system used to control on-flow conditions. The leading edge of the wing is located at $\mathbf{x} = (\mathbf{0.97}, \mathbf{0}, \mathbf{0})$). The flapped system introduces an onflow

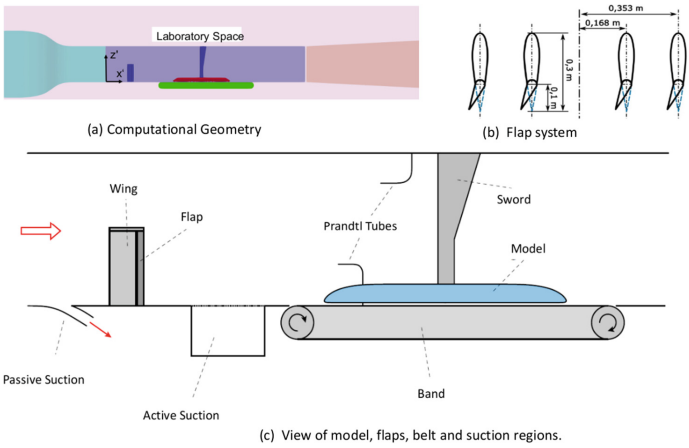

Fig. 1. (a) The computational domain in the x-z symmetry plane of the wind tunnel. The wind tunnel co-ordinate system, shown at the start of the test section, is used for both experiment and CFD. (b) The flap system is aligned with the tunnel symmetry axis. (c) Components of the experimental setup are illustrated.

condition represented by controlled oscillations about the mean train velocity. For the present work, the term "stationary flap" indicates a non-oscillating flap fixed in at the minimum drag (or neutral) position. The flap is described using the parameters of frequency (30 Hz.) and amplitude (3°) of oscillation. Figure 1(c) illustrates the model positioned in the wind tunnel test section over the moving belt. The train nose is positioned at $\mathbf{x} = (\mathbf{0.97}, \mathbf{0}, \mathbf{0})$. The moving belt velocity matches the bulk on-flow velocity which simulates an inertial reference system moving at this velocity. The model is an 1:25 scale NGT-Cargo train with a center wagon and two end wagons. The length of the model is 2.58 m. The model train height (L_h) is 200 mm. The train base has a width (L_b) of 125 mm. The reference area of the model (given by the projected area of the train head in the mean flow direction) is 0.02 m^2. Passive/active suction removes the boundary layer approaching the flaps and model and allows the experiment to better match a moving reference system with no mean oncoming wind. A passive ventilation system, driven by the local pressure differential between the wind tunnel interior and exterior, is located upstream of the flap system. An additional active system, driven by a compressor, is located in front of the moving belt. Suction removes the oncoming boundary layer which is consistent with an inertial reference frame moving at the train velocity. The head of the static probe shown in the figure are 400 mm above the tunnel floor or the belt. The definition of the characteristic length for the Reynolds number typically uses a reference width of 3 m at full scale in Europe. The scaled reference width provides the reference length used to compute the Reynolds number for the wind-tunnel experiment. The Reynolds number is defined as

$$R = \rho L_b U / \mu, \tag{1}$$

where U, ρ, μ, and L_b are the free stream velocity, the fluid density, the fluid dynamic viscosity and the Reynolds length scale respectively. For this work the Reynolds number, which is based on L_b, is 200,000 for the selected test section bulk velocity of 30 m/s (U_{ref}). Both the reference pressure and temperature varies slightly about 101325 Pa. and 298.5 °K respectively. Table 1 shows the set of experimental configurations selected from the experimental program for comparison against the CFD. A complete description of the measurement system used in the experiments is not within the scope of this paper but can be found in [15] and references therein. The wind tunnel turbulence level is approximately 0.15%. Spatial and temporal variations of the test section velocity profile are less than 0.5% with errors in both steady and unsteady force measurements being comparable. The pressure gradient across the head and tail of the model is of the order of three Pascals per meter. A description of the measured test conditions against which the CFD has been compared can be seen in Table 1.

Table 1. Test conditions against which CFD results are compared. Measured drag counts for the model (dcnts) are provided. At present only the RMS drag count for experiment 0047 is available. All experiments (except 0018) use the moving belt.

Experiment	Passive Suction	Active Suction	Flaps/Freq. (Hz.)	dcnts	rms(dcnts)
0018	Off	Off	No/NA	43	-
0020	Off	On	No/NA	47	-
0021	On	Off	No/NA	45	-
0022	On	On	No/NA	48	-
0023	On	Off	Yes/0	44	-
0024	On	On	Yes/0	49	-
0047	On	On	Yes/30	50	3

3 The Numerical Method

The current work uses the Engys OpenFOAM releases 3.5.0/3.5.1. Justification for use of the incompressible form of the Navier-Stokes equations is provided by the Mach number of the wind-tunnel flow (M = 0.09). Turbulence effects are conventionally modeled using an effective viscosity model [18]. For RANS solutions the Semi Implicit Method for Pressure Linked Equations (SIMPLE) [17] algorithm is used. Unsteady calculations use the Pressure Implicit Method with Splitting of Operators (PISO) [22]. The Courant-Friedrichs-Lewy (CFL) number is limited to O(1), leading to time steps of the order 10^{-6} s for unsteady calculations. The discrete operators are second order in both space and time. Steady solutions are terminated when the residuals of the pressure correction equation, momentum equations, and turbulent viscosity equations are of O(1e-10, 1e-8, 1e-7) respectively. This convergence criterion is also used for the unsteady calculations however an additional check is used to assess when the averaged drag vector variation lies within a 99% confidence interval (CI) about an error of

1.0e-6 drag units. Based on the comparative performance of other turbulence models for similar problems [9–11] the baseline turbulence model chosen is the Menter k-ω SST turbulence model [19]. The hybrid RANS-LES calculations use the Delayed Detached Eddy Simulation (DDES) version of this turbulence model [20]. The DDES filter width chosen as 2Δ [23], where Δ is the cube root of the cell volume. Approximately 60–70% of the total turbulent kinetic energy is resolved. The intention is to reduce dissipation effects inside vortex cores and free-shear layers without impacting on computational costs. A blended form of the inviscid flux operator is used to assist in reducing numerical dissipation effects for hybrid RANS-LES. Boundary conditions are specified in [9]. In this paper a drag count (dcnt) is defined as $1000C_d$ where C_d is the drag force normalized by the product of the reference dynamic pressure and the reference area. Wall clock time for these calculations scale at about 5.0e-4 s per grid point per iteration on the DLR CARO cluster.

4 The Computational Mesh

It is considered that the presence of significant vortical and separated flow regions about the train (under-body, inter-car gaps) require additional refinement and the train model was embedded inside a high resolution refinement block. The refinement block extends from $6L_b$ upstream of the train head to $30L_b$ downstream of the train tail respectively. The height of the refinement block is set at $2L_h$. Surface length scales are of O(2) mm, while control volume length scales vary from 2 mm near the vehicle to 15 mm inside the wind tunnel space. Wake regions for the flaps are resolved to a length scale of 3 mm up and including the refinement block. Specification of the mesh near-wall resolution (in terms of y+) follows [9] however y+ was reduced by a factor of two and the mean value of y+ about the model was set to y+ 16. The concept of an optimum y+ implies that near wall numerical solutions are representative of near wall physics. The wall function models used in this work replicate zero and mild pressure gradient boundary layer behavior sufficiently well but are expected to deviate from experiment for unsteady flows with stronger unsteady adverse pressure gradient and streamline curvature effects. Investigation of a universal wall function approach is not within the scope of this investigation however these calculations fall within the envelope of published industrial applications.

5 Assessment of the Computed Flow Fields

Current CFD assessments of the integral forces are given in Table 2. This table is divided into 6 groups with first 5 groups representing the CFD cases computed, while the last presents data derived from the experiments. Data sets (m1, m2, ...) are denoted here as M(m1, m2, ...). By comparing M(0018,0020) it can be seen that active suction with a moving belt increases the measured model drag by 4 dcnts. This observation is consistent with M[0023,0024], which includes the additional influence of a stationary flap system. The active suction increases the

Table 2. Comparison of the drag force estimates returned by the CFD.

Case	CFD Method	Matching Experiment	dcnts	rms(dcnts)
A	RANS	0018	52	-
B	RANS	0020	56	-
C	URANS	0024	69	1
D	DDES	0024	57	1
E	DDES	0047	59	4

model drag by 5 dcnts. The mean drag count differences between M[0018,0021] and M[0020, 0022] suggest that passive suction increases the model drag count by 1.5 dcnts on average. Application of passive and active suction could introduce changes of up to 6.5 dcnts. Comparison of M(0018,0020) and M(0023,0024) suggests that the moving belt increases the drag by 4 to 5 dcnts. M[0021,0023] and M[0022,0024] indicate that the stationary flap system reduces drag by 1 dcnt. This is expected since the flap generated wake fields which partially block the model's onflow (see Figs. 2 and 3). Differences in drag for M[0021,0023] shows an reduction of 1 drag count due to the presence of the stationary flaps, however activation of the moving belt for M[22,24] increases the drag count by one for this configuration. The moving belt and passive/active suction mechanisms remove the oncoming boundary layer so that the modeled drag coefficient will increase - this is seen in the experimental data. Neglecting the passive/active suction mechanisms can introduce an error of about 6 dcnts with an additional error of up to 5 if no moving belt is present.

The CFD results are compared against the EN 14067-6 standard (despite the fact that the standard is accepted for RANS only). The experimental values are considered as reference values for the remainder of this paper since they are the only independent source for comparison against the CFD. The percentage difference of the CFD against a reference value is presented together with the drag count as a data pair (represented by E[dcnts, percentage difference]). Calculation A is a RANS calculation based on the Menter-SST turbulence model. No boundary layer removal mechanisms are modeled. Differences for the pair M[A,0018] are given by E[9,20]. Calculation B uses a RANS method however the moving belt system is now modeled. Differences between [B,0020] are given by E[9,19]. This is comparable to the difference between M[A,0018]. However drag differences between M[A,B] and M[0018,0020] are 4 dcnts respectively. Groups (C) and (D) evaluate the effect of an improved physical models with the moving belt included together with the flaps fixed in the neutral position. Comparison of M[C,0024] returns E(22,47) for the URANS result while the comparison M[D,0024] returns E[8,16] for the DDES method. This result is consistent with other studies which suggest that flow resolving methods should be obligatory for these calculations. In further discussions non-resolved calculations (A,B,C) are discarded. M[E,0047] returns E(9,18) while the differences between M[D,E] and M[0024, 0047] are two dcnts and one dcnt respectively. This illustrates a typical

observation in industry: CFD results are usually more accurate in estimating drag deltas across design changes then when comparing a drag assessment at a single design condition. Industrial flows are highly complex. The simplifications required to make cost effective numerical methods for these flows can introduce systematic errors. These errors appear to cancel when differences between solutions (based on identical numerical schemes) are computed. The observed error in neglecting both passive and active suction (6.5 dcnts) suggests that, if these are included in the CFD model, the drag count differences between CFD and experiment could be reduced to less than 4 dcnts with the certification standard used in this paper being achieved.

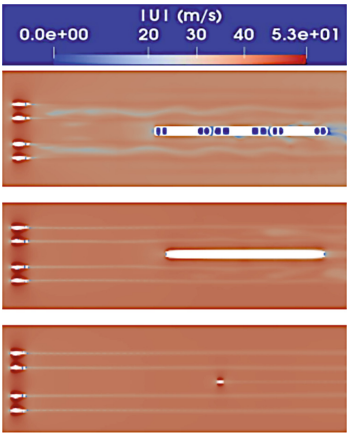

Fig. 2. In the figure the wake development behind both the stationary flap system is shown. Upper figure: $z/L_h = 0.2$; Middle figure: $z/L_h = 0.94$; Upper figure: $z/L_h = 2.4$.

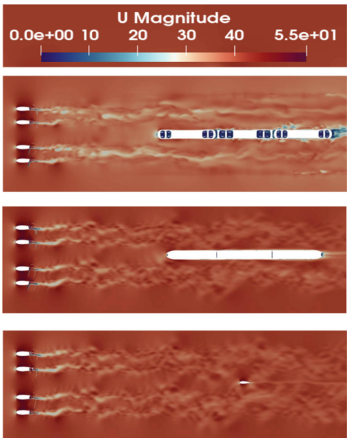

Fig. 3. In the figure the wake development behind both the oscillating flap system is shown. Upper figure: $z/L_h = 0.2$; Middle figure: $z/L_h = 0.94$; Upper figure: $z/L_h = 2.4$.

Figure 2 illustrates the wake development downstream of the stationary flap at three different values of height above the wind-tunnel floor. Close to the wind tunnel floor the twin wakes, seen to the left and right of the symmetry axis, merge. The model is then bounded by two merged wakes to the left and right of the model's symmetry axis. As distance from the floor is increased the wake interactions with the model reduce until the wake travels undisturbed through the test section. The situation changes when the flaps oscillate as can be seen in Fig. 3 where significant interaction between the wakes and the model are seen. This figure shows that the left and right wake pairs have not merged into two pairs. Investigations of the flow field at other time instances suggest that wake merging is time dependent which adds additional disturbances to the onflow

condition. Both figures show evidence of interaction between the flow and ICG's and under-body.

Figure 4(a) shows the computed power spectral densities for the computed drag force components (case D). The spectra are averaged over 30 convective time units with a low pass Hanning filter being applied. Similar post-processing is also applied to the experimental data. At the time of writing the measured force time series for cases with the steady flaps requires additional post-processing and direct comparison of measured and computed spectra will be provided in later work. All force components exhibit a peak 3 Hz (St = 0.007) with indications of higher harmonics of up 9 Hz (St = 0.07). F_z shows a peak at 25 Hz (St = 0.12) while F_y contains two modes at about 12 (St = 0.06) 45 Hz (St = 0.23). T25 Hz peak is believed to relate to the moving belt. A timescale derived from the model length and U_{ref} matches 12 Hz (St = 0.06) mode implying that this mode is flow related. however this mode matches the rotational Eigenfrequency of the model-spear combination suggesting coupled flow-structure interaction. T45 Hz (St = 0.22) mode is close to the Strouhal number observed for vortex shedding about bodies of aspect ratio greater than 2, however the CFD overestimates this mode by about 14% which is characteristic for non-resolving methods. Figure 4(b) illustrates the development of the fluctuating aerodynamic force coefficients over 25 convective time units. Since $L_b = 1/8$ m and both the forcing frequency and the bulk velocity share the same magnitude (30 Hz/30 m/s), a total angular rotation of 2π radians corresponds to eight convective time units and it is easy to see that the period of F_Y is slightly shorter than the flap oscillation frequency. As noted earlier the CFD results show that wakes dynamically interact downstream of the flaps, thus adding additional dynamic processes which influence the model's aerodynamic force response. However the aerodynamic forces respond directly to on-flow changes, supporting the observations of [14,15] and [16].

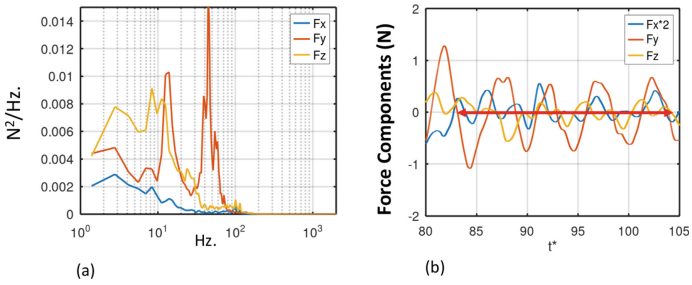

Fig. 4. (a) Power spectral density of the model's aerodynamic force components. (b) A time interval sample of the model aerodynamic force development under an unsteady onflow condition created by the flapped system. Note that $t* = tU/L_h$ is the time normalized by the flow convective time unit based on model height.

6 Conclusions

Investigations are undertaken to validate CFD methods against experiments by studying the influence of a time-dependent inflow on the aerodynamic drag of a 1:25 scaled model train. Both steady and unsteady on-flow conditions are considered. An oscillating flap system is used to control the amplitude and frequency of the on-flow oscillations. Non-resolving DDES methods shows superior performance to URANS at an equivalent computational cost. Drag changes predicted by the CFD due to changes of the computational model (inclusion of flaps and moving belt) closely match measured drag changes. An analysis of the experimental data suggests that the inclusion of the active/passive suction into the CFD model will reduce the difference between CFD and measurements. The fluctuations in computed drag match measured the fluctuation under unsteady onflow conditions. The CFD indicates that wake interactions upstream of the model can occur. These interactions should have the potential to generate additional flow dynamics (which are not yet understood) and will influence the aerodynamic forces frequency response to the upstream flow. The flow examined is highly complex and the CFD appears to contain systematic errors which make it difficult to return accurate drag assessments at arbitrary onflow conditions. Future research will need to identify and remove these systematic errors while retaining an efficient numerical method. The next step is in this work is to include both passive and active suction into the computational model. An important observation arising from this work is that CFD and experiment are complementary in achieving a deeper understanding of these flows.

Acknowledgment. The authors would also like to acknowledge Frau Annika Köhne for her assistance in the preparation of this paper. The resources of the Cluster for Advanced Research in Aerospace (Dresden (CARA), Göttingen (CARO)) are used for the work presented in the paper.

References

1. Baker, C.: The flow around high speed trains. J. Wind Eng. Ind. Aerodyn. **98**(6), 277–298 (2010)
2. Orellano, A.: Aerodynamics of High Speed Trains. Vehicle Aerodynamics lecture, Stockholm KTH (2010)
3. DB Netz AG., Richtlinie 807.04 Bautechnik, Leit-, Signal- und Telekommunikationstechnik: Ausgewählte Maßnahmen und Anforderungen and das Gesamtsystem Fahrweg/Fahrzeug Aerodynamik/Seitenwind, Frankfurt (2010)
4. Sima, M., Gurr, A., Orellano, A.: Validation of CFD for the flow under a train with 1:7 scale wind tunnel measurements. In: BBAA IV International Colloquium on Bluff Bodies Aerodynamics and Applications (9), pp. 1638–1649 (2008)
5. Jönsson, M., Wagner, C., Loose, S.: Particle image velocimetry of the underfloor flow for generic high-speed train models in a water towing tank. Proc. Inst. Mech. Eng. Part F J. Rail Rapid Transit **228**(2), 194–209 (2014)

6. Muld, T.W.: Slipstream and flow structures in the near wake of high-speed trains. Royal Institute of Technology, Department of Aeronautical and Vehicle Engineering, Stockholm, Sweden (2012)
7. Baker, C.: A review of train aerodynamcics: part 1 - fundamentals. Aeronaut. J. **118**(1201), 201–228 (2014)
8. Hemida, H.N.: Large-Eddy Simulation of the Flow around Simplified High-Speed Trains under Side Wind Conditions, Engng, Division of Fluid Dynamics, Dept. of Applied Mechanics, Chalmers University of Technology, Göteborg, Sweden (2006)
9. Weinman, K.A., et al.: Assessment of the mesh refinement influence on the computed flow-fields about a model train in comparison with wind tunnel measurements. J. Wind Eng. Ind. Aerodyn. **179**, 102–117 (2018)
10. Weinman, K.A, Fey, U., Loose, S., Wagner, C., Deiterding, R., Fragner, M.: Comparison between CFD and Wind Tunnel experiment for slender bodies of aspect-ratio O1 in the presence of cross-wind. In: 10th World Conference on Railway Research (2013)
11. Fragner, M.M., Weinman, K.A., Deiterding, R., Fey, U., Wagner, C.: Comparison of industrial and scientific CFD approaches for predicting cross wind stability of the NGT2 model train geometry. Int. J. Railways Technol. **4**(1), 1–18 (2015)
12. Haff, J., Richard, U., Kowalski, T., Loose, S., Wagner, C.: Wind tunnel experiments with a high-speed train model subject to cross-wind conditions. In: Proceedings on the First International Conference on Railway Technology: Research, Development and Maintenance (24), J. Pombo, Civil-Comp Press, Stirlingshire, Scotland (2012)
13. Fragner, M.M., Deiterding, R.: Investigating cross-wind stability of high speed trains with large-scale parallel CFD. Int. J. Comput. Fluid Dyn. **30**(6), 402–407 (2016)
14. Wilhelmi, H., Jessing, C., Bell, J., Heine, D., Wagner, C., Wiedemann, J.: Aerodynamic characterisation of a compact car overtaking a heavy vehicle. In: Dillmann, A., Heller, G., Krämer, E., Wagner, C., Tropea, C., Jakirlić, S. (eds.) DGLR 2018. NNFMMD, vol. 142, pp. 794–804. Springer, Cham (2020). https://doi.org/10.1007/978-3-030-25253-3_75
15. Wilhelmi, H., et al.: Simulation of transient on-road conditions in a closed test section wind tunnel using a wing system with active flaps. SAE Int. J. Passeng. Cars Mech. Syst. (0688), 1–13 (2020). ISSN 1946-3995
16. Weinman, K.A., Wilhelmi, H., Bell, J.R., Heine, D., Wagner, C.: On the simulation of a heavy vehicle wake in OpenFOAM with real-world data. In: Dillmann, A., Heller, G., Krämer, E., Wagner, C. (eds.) STAB/DGLR Symposium 2020. NNFMMD, vol. 151, pp. 504–513. Springer, Cham (2021). https://doi.org/10.1007/978-3-030-79561-0_48
17. Patankar, S.V., Spalding, D.B.: A calculation procedure for heat, mass and momentum transfer in three-dimensional parabolic flows. Int. J. Heat Mass Transf. **15**(10), 1787–1806 (1971)
18. Wilcox, D.C.: Turbulence Modeling for CFD, 3rd edn. DCW Industries, Canada, CA, USA (2006)
19. Menter, F.R., Kuntz, M., Langtry, R.: Ten years of industrial experience with the SST turbulence model. In: Proceedings of the 4th International Symposium on Turbulence, Heat and Mass Transfer, Begell House Inc., West Redding, pp. 625–632 (2003)
20. Strelets, M.: Detached eddy simulation of massively separated flows. In: 39th AIAA Aerospace Sciences Meeting and Exhibit, Reno, NV (2001)
21. Bardina, J.E., Huang, P.G., Coakley, T.J.: Turbulence modeling validation, testing, and development. NASA Technical Memorandum, vol. 110446 (1997)

22. Issa, R.I.: Solution of the implicitly discretized fluid flow equations by operator-splitting. J. Comput. Phys. **62**, 40–65 (1985)
23. Weinman, K., et al.: A study of grid convergence issues for the simulation of the massively separated flow around a stalled airfoil using DES and related methods. In: Wesseling, P., Oñate, E., Périaux, J. (eds.) Proceedings of the European Conference on Computational Fluid Dynamics ECCOMAS CFD 2006, Egmond aan Zee, The Netherlands (2006)